Journal Pre-proofs

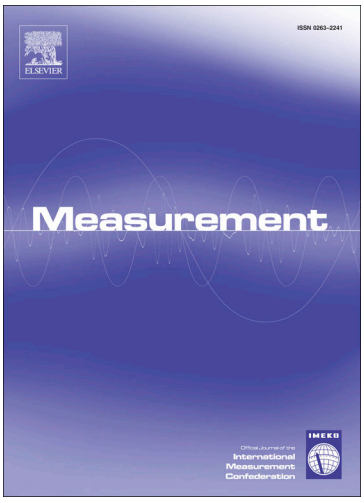

Experimental uncertainty decompositions of aerodynamic coefficients affected by operative condition variations

Ander Zarketa-Astigarraga, Alain Martin-Mayor, Manex Martinez-Agirre

PII: S0263-2241(20)30479-6
DOI: https://doi.org/10.1016/j.measurement.2020.107941
Reference: MEASUR 107941

To appear in: *Measurement*

Received Date: 23 January 2020
Revised Date: 24 April 2020
Accepted Date: 6 May 2020

Please cite this article as: A. Zarketa-Astigarraga, A. Martin-Mayor, M. Martinez-Agirre, Experimental uncertainty decompositions of aerodynamic coefficients affected by operative condition variations, *Measurement* (2020), doi: https://doi.org/10.1016/j.measurement.2020.107941

Experimental uncertainty decompositions of aerodynamic coefficients affected by operative condition variations

Ander Zarketa-Astigarraga[a,*], Alain Martin-Mayor[a], Manex Martinez-Agirre[a]

[a] *Mondragon Unibertsitatea, Faculty of Engineering, Mechanical and Industrial Production, Loramendi 4, Mondragon 20500 Gipuzkoa, Spain*

Abstract

A twofold analysis is performed on an experimental set-up comprising a low-Reynolds wind tunnel, with the aim of quantifying the effect of measurand uncertainties and operative condition variations in the lift and drag curves of a NACA0021 airfoil. The first part of the study focuses on an uncertainty analysis of basic measurands used for calculating standard aerodynamic magnitudes, showing the individual contributions of each of the factors affecting the overall uncertainty ranges. The second part intends to show how those uncertainties are propagated to lift and drag coefficients, and to calculate the effect of varying operative conditions on those curves. It is found that, when changes in operative conditions are left unattended, their influence on derived magnitudes may grow as large as to cause the resultant data to lie outside the estimated uncertainty intervals. Additionally, those variations are shown to depend non-linearly on the operative condition changes that produce them.

Keywords: uncertainty analysis, operative conditions, wind tunnel, lift and drag coefficients

(∗) Corresponding author

() *Email address:* azarketa@mondragon.edu (Ander Zarketa-Astigarraga)

1. Introduction

The main purpose of physical experimentalism is the replication of phenomena not occurring in nature in ways that allow their proper investigation. The limitations may be traced back to two principal causes: on the one hand, the number of physical processes taking place on a particular scenario and the interrelations among them do not allow isolating a particular phenomenon adequately. On the other hand, a phenomenon may manifest solely under certain physical conditions that are not naturally observable in a sufficiently sustained manner so that an analysis can follow. The field of physical experimentalism overcomes those limitations by means of building experimental set-ups—physical scenarios within which particular phenomena are reproduced in an artificial manner and, ideally, free of spurious disturbances. Specifically designed apparatus are employed to manipulate the medium in order to set the proper physical conditions, and the background is adapted so that processes affecting the phenomenon are suppressed or, at least, attenuated. It is under these controlled conditions that experimental tests are performed.

Ensuring controlled conditions within a given experimental set-up requires quantifying the achieved artificial configurations somehow. When undertaking a test, the usual workflow consists of setting a number of input magnitudes to predefined values and measuring a set of output parameters. Evidently, the output values are inherently dependent on the input magnitudes. However, the latter are not to be interpreted solely as a sort of boundary conditions of the experimental set-up. In fact, both input and output datasets come from measurements performed during a test, and the probes or sensors used for measuring the magnitudes may be subjected to a number of uncertainty sources. Those sources, if unaccounted for, can deprive the test of its controlled condition status. This, in turn, affects possible correlations that may exist between input and output parameters, as wrongly controlled inputs can lead to outputs that do not match with expected values, may these come from theoretical predictions or empirical relations. In any case, a rigorous consideration of the uncertainty sources influencing both input and output magnitudes is mandatory if experimental relevance is to be achieved.

The different uncertainty sources encountered in an experimental set-up may be divided in two main groups. The first group considers the uncertainties coming from the physical limitations of the probes and their interactions with the overall system. The physical limitations are constrained by the sensitive part of the probe, which is able to detect changes on a given physical magnitude as far as those changes lie above a probe-dependent threshold, or resolution; besides, input signal conversions, such as digitalizing processes, may introduce deviations on the measurements or even widen the resolution level of the sensor due to the addition of noise or scattering. Lastly, it is to notice that the probe itself constitutes a physical system that, even if small in comparison to the characteristic dimensions of the experimental set-up, is intrusive to some extent. These unavoidable interactions with the experimental medium may alter the magnitudes to measure, and their effects need to be considered accordingly. A statistical approach towards a systematic quantification of the mentioned uncertainties is set forth by the theory of uncertainty analysis, whose basic notions are detailed further on. The readers seeking deeper insights may consult the canonical references on the subject [1–5], whereas an updated version gathering the relevant aspects of the theory is to be found in [6].

The second group of uncertainties is related to the changes that the experimental set-up may suffer due to its operative conditions. The apparatus employed for reproducing a phenomenon by forcing the physical conditions can cause significant variations in magnitudes that affect the phenomenon indirectly, thus introducing unexpected side effects. The way of dealing with such effects calls for identifying the overall set of both primary and secondary magnitudes that affect the phenomenon; ideally, achieving controlled conditions requires measuring those magnitudes and setting them to user-defined values. However, experimental set-ups do not always allow a direct manipulation of the overall set of physical magnitudes, and changes due to operative conditions are to be merely assumed, not user-set. Even in these cases, the requirement of measuring the overall set of parameters is not relaxed. Instead, the influence of the operative conditions is to be assessed by performing a proper uncertainty analysis of the affected magnitudes and propagating those uncertainties to the output parameters. If the changes due to operative conditions introduce unacceptable deviations in the outputs, it turns necessary to control the test by simultaneously monitoring the input parameters together with the magnitudes affected by those operative conditions.

The present paper aims at analysing the influence of the mentioned uncertainty sources in a particular experimental set-up, namely a low-Reynolds wind tunnel [7]. The analysis focuses on the characteristic curves of lift and drag coefficients obtained for a standard NACA airfoil, and on the influences that the uncertainty intervals of the probes and the operative conditions may exert on them. Such curves are commonly used as design and prediction tools of airfoils. This is so because they represent the variations of lift and drag coefficients with the main operative parameter, the angle of attack, which is the one standing between the chordwise direction and the incoming flow. Besides, the dependency of those curves on the Reynolds number is a well-established fact [8]; in aerodynamic studies, its value determines the fluid regime being developed along the body and, ultimately, the fluid structures responsible of lift and drag values. The low-Reynolds configurations tested herein make the flow stand in the so-called transitional regime, where the dependency of the coefficients on the Reynolds number is most sensitive [9], and a precise uncertainty analysis on it becomes essential. Additionally, the Reynolds number is dependent on several flow-dependent properties, which are shown to be affected by operative conditions in the case of open circuit tunnels, apart from owning a specific uncertainty interval due to the interrelation of measurements coming from different probes. The undertaken approach intends to show the importance of controlling the current experimental set-up with the aim of keeping a constant Reynolds number during the tests. It is to bare in mind that those tests may last long enough as for allowing the tunnel to introduce severe operative changes. Disregarding such control, on the other hand, is shown to be liable to introduce deviations that grow beyond an acceptable experimental error.

The paper is structured as follows. Section 2 provides a concise theoretical background on the theory of uncertainty analysis and introduces some specific terminology related to it, in order to facilitate further explanations on the subject. Section 3 details the current experimental set-up, both the apparatus employed for obtaining a controlled airflow and the set of probes used in the measurements. Section 4 presents the results of the tests and the corresponding discussions, and is divided in two parts: Section 4.1 verses on the uncertainty analysis performed on the set of probes and on how the uncertainties of basic measurands are propagated to derived results; Section 4.2 highlights typical operative condition changes found on standard lift and drag tests performed on the present wind tunnel, and shows how those changes affect the computed results. Finally, Section 5 summarizes the main findings of the analysis.

2. Theoretical background on uncertainty analysis

The uncertainty analysis undertaken herein is based on the notion of replication levels [2–5], which provides a systematic approach towards accounting for the set of possible error sources that may deviate the measured value from the true value of a magnitude. These deviations, as different in nature as they might be, are conceptualized as perturbation terms that enter the so-called measurement chain [2, 3]. This chain links the hypothetical true value of a magnitude and the final value that the experimentalist employs on the description of the phenomenon. The main idea behind the concept of replication levels is that the experimentalist is able to perform uncertainty tests on probes under conditions that avoid the introduction of certain error sources in the measurements. This, in turn, allows quantifying the effect of the remaining uncertainties on a statistical basis. Thus, the systematic approach laid by the replication level philosophy aims at quantifying those uncertainties following a bottom-up scheme of generality on the assumptions that the experimentalist may make regarding the presence of different error sources.

The simplest scenario regarding the measurement process is to assume that time itself is frozen [3], i.e. that what is being analysed is a picture of the scaled display of the device, and not a temporal evolution of the magnitude. This is analogous to considering that the only potential source of error present in the measurements is the scale-reading interpolation at the resolution level of the device. On a human-read analogic display, it corresponds to the different readings that several experimenters would perform of the same picture. On a machine-read digital device, the round-off operation of the display may be affected by small perturbations coming from the elctrical circuitry or from equilibrium thermodynamic fluctuations. This scenario is termed the 0^{th} order replication level, and is to be assessed with the experiment at issue not running. Its main purpose is to provide information on the suitability of a given probe with respect to the measurements it is to perform.

The 1^{st} order replication level considers the probe on its measurement configuration, with the physical phenomenon of interest taking place. The finite dimensions of the probe alter the system within which it is placed, and those system perturbations may deviate the measured value from the true value. Additionally, as the probe itself is a system on its own, its interactions with the surroundings, termed system/sensor interactions, also affect the measured value. Both of these interactions are accounted for by analytical-empirical correlations. The third type of detectable perturbations, namely timewise fluctuations that are larger than the sensitivity of the probe, are calculated by undertaking specifically designed tests for each probe that allow measuring the timewise scatter present on the output data. The resultant uncertainty intervals serve to diagnose data coming from the same experimental set-up and detecting mislead measurements due to unexpected changes on testing grounds, such as excessive variations introduced by operative conditions.
The N^{th} order replication level considers, in addition to the previous terms, the uncertainties coming from manufacturing defects, sensitive material inhomogeneities or several sources alike, which are due to the fabrication process previous to the acquisition of the device by the final user. This category also comprises, as part of the sources that come from the manufacturer, possible measurement errors committed during the calibration process. Those two factors account for the fact that this replicability order is not reproducible on experimental tests. Instead, the value of the calibration uncertainty is meant to be estimated from the technical datasheets of the devices. The uncertainty intervals resultant from the N^{th} order replication level are meant to be part of the final data report, as they serve as comparative indicators among similar tests performed in different experimental set-ups.
As it stands, the replication level approach allows computing the different uncertainty intervals that come to affect the set of basic measurands comprising a given experimental test. However, it does not indicate how different intervals affecting the same measurand are to be combined to yield an overall uncertainty descriptor of that measurand. Neither does show, besides, how to quantify the uncertainty intervals of derived magnitudes, which are the ones not directly measured in the test, but obtained by functional relations among basic measurands or other derived magnitudes. With all, the computation of basic uncertainty intervals is performed by tools of statistical inference and, hence, each of such intervals is given a so called confidence level. This confidence level represents the probability of additional measurements yielding values that fall outside the interval it is ascribed to. As such, the theory of uncertainty analysis states that the combination of uncertainties of different sources that affect a particular magnitude is to be performed on a probability-preserving manner [1]. The experimentalist, as such, is free to choose a judicious confidence level for each of the uncertainty intervals of basic measurands. What the probability-preserving philosophy states is that one such confidence level is to be chosen for the set of basic measurands, in which case it is possible to propagate it to the derived magnitudes. In other words, what is sought is that the overall set of uncertainty intervals shares a common confidence level. In the end, an experimentally measured generic magnitude ϕ is to be expressed as:

$$\phi = \overline{\phi} \pm \delta\,(1:b)\,, \tag{1}$$

where $\overline{\phi}$ is the best estimate of the magnitude, and matches its mean value, δ is the computed uncertainty interval, and $(1:b)$ is directly related to the user-defined confidence level. A value of 95% is typical for this level, for which b equals 20, and such a convention is employed in the measurements performed herein. On probabilistic grounds, the $(1:b)$ expression means that the experimentalist is confident that, when repeating an experiment b times, the resultant dataset of b values is probable to own just a single instance that falls outside the reported uncertainty interval. Regarding the calculation of the overall uncertainty value (δ), Kline & McClintock [1] provide the following expression:

$$\delta = \sqrt{\sum_{i=1}^{i=N} \left(\frac{\partial \phi}{\partial x_i} \delta_{x_i} \right)^2}\,, \tag{2}$$

where ϕ depends on a number N of magnitudes represented by the generic x symbols, each of those x_i owning a particular uncertainty interval δ_{x_i}, which itself is calculated applying Equation (2) to that particular magnitude x_i. This recursive method stops at the innermost level of the measurement process, when dealing with basic measurands, whose individual contributions are directly computed from the tests corresponding

to the replication levels.
Thus, the uncertainty analysis approach presented herein takes the form of a systematic scaffolding towards the quantification of uncertainty intervals of physical magnitudes. The tests corresponding to replication levels serve to calculate individual contributions that affect basic measurands, from which their overall uncertainty intervals are computed. The intervals of derived magnitudes are related to the intervals of the measurands they depend on by means of Equation (2). This equation shows that the uncertainty analysis of any derived magnitude can be traced back to the deviations that affect the basic measurands.

3. Experimental set-up

The physical scenario (see Figure 1), namely the low-Reynolds wind tunnel, is a suction-type tunnel owning a rectangular cross-section of 0.75×1 m^2 and a length of 3 m; maximum wind speeds of 40 m/s are achievable at the test-section, with the background turbulence level not surpassing a 0.2% value.

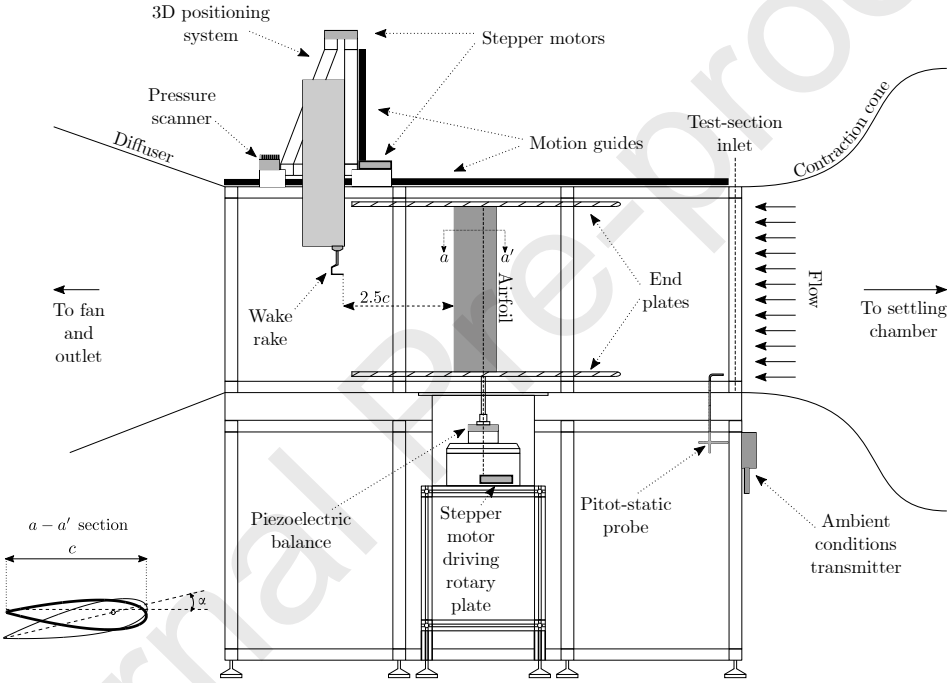

Figure 1: schematic sketch of the experimental set-up. The depicted configuration shows the layout of the devices for obtaining characteristic lift and drag curves for the NACA0021 airfoil. The flow, coming from right to left, is confined within two end-plates for ensuring two-dimensionality. The ambient conditions transmitter and the Pitot-static probe serve for measuring and controlling the Reynolds number at the inlet; the piezoelectric balance and the wake-rake device are used for obtaining the data that, when post-processed, provide the lift and drag coefficients, respectively. The $a - a'$ section intends to depict the geometrical shape of the NACA airfoil, as well as indicating how the angle of attack (α) is defined.

The set of basic measurands are classified in two groups: the ones employed for characterizing the airflow, and the ones describing the airflow-airfoil interactions. The former group includes four measurands: the atmospheric pressure (p_{amb}), the ambient temperature (T_{amb}), the relative humidity (RH) and the inflow velocity (V_∞). The second group contains two additional descriptors: loads exerted upon the airfoil, represented by a force vector ($\mathbf{F} = (F_x, F_y, F_z)$), and pressure measurements performed either on the surface of the airfoil or in the perturbed flowfield (p). These measurands are obtained by a set of four sensors, whose relevant specification parameters are gathered in Table 1.

(1) max. sampling-frequency achievable.

The set of derived magnitudes includes: the corrected velocity (V_∞^{corr}), obtained when applying the correspondent pressure and temperature corrections to the raw data coming from the Pitot-static probe; air density and viscosity (ρ_{amb} and μ_{amb}) calculated employing the moist air state equations of those variables [10, 11]; inflow dynamic pressure ($q_\infty = \rho_{amb}\left(V_\infty^{corr}\right)^2/2$); Reynolds number based on the airfoil's chord c ($\mathrm{Re} = \rho_{amb}V_\infty^{corr}c/\mu_{amb}$); and lift and drag coefficients, both uncorrected (C_L and C_D) and corrected (C_L^{corr} and C_D^{corr}) for tunnel wall effects following Selig et al. [12]. The airfoil, namely a NACA0021, owns a chordwise dimension of 150 mm and a span (s) of 900 mm. Figure 2 provides a schematical view of the hierarchy resultant from the functional relation of derived magnitudes with respect to either basic measurands or other derived magnitudes, and the uncertainty analysis to be performed at each level.
It is to remark that lift and drag coefficients are obtained differently (see Figure 3): the lift coefficient is calculated by directly measuring the lift force on the airfoil and non-dimensionalizing it with $q_\infty{\cdot}s{\cdot}c$. Due to the difference in the orders of magnitude of lift and drag loads and the inherent coupling among the piezoelectric's axes, the drag coefficient is obtained by the so-called momentum deficit method [8, 13, 14].

(2) the probe is differential, and owns a [0, 1000] Pa range.
(3) dependent on ambient conditions; the provided value is for calibrated conditions.
(4) digital display with 2 decimal units.
(5) settable.
(6) settable; dependent on amplifier mode.
(7) dependent on measurement channel and configuration.

Table 1: set of probes for basic measurand readings.

Measurand(s)		Device alias/*model*	Parameters	Values
Ambient conditions	p_{amb}	**Ambient conditions transmitter** *Delta-Ohm HD2001.1*	Full-scale range Accuracy Resolution	$[600, 1100]$ mbar $\pm 0.1\%$ FS $= \pm 0.5$ mbar 0.01% FS = 0.05 mbar
	T_{amb}		Full-scale range Accuracy Resolution	$[-20, 80]$°C $\pm 0.3\%$ FS $= \pm 0.3$°C 0.05% FS = 0.05°C
	HR		Full-scale range Accuracy Resolution	[0, 100]% $\pm 2\%$ FS $= \pm 2\%$ 0.05% FS = 0.05%
	Common		Dynamic response(1)	0.125 sec (8 Hz)
Inflow velocity	V_∞	**Pitot-static probe** *Delta-Ohm HD49047T01L*	Full-scale range(2) Accuracy Resolution(4) Dynamic response	41.75 m/s(3) $\pm$ 1% FS = 0.4 m/s 0.0012% FS = 0.005 m/s 0.05 sec (20 Hz)
Loads	**F**	**Piezoelectric balance** *Kistler 9119AA2*	Max. full-scale range(5) F_x, F_y, F_z Sensitivity F_x, F_z Sensitivity F_y	± 4 kN $\approx$ -26 pC/N $\approx$ -13 pC/N
	Misc.		Natural frequencies f_{N_x}, f_{N_y}, f_{N_z} Resolution Dynamic response(6) Electrical drift(7)	≈ 6 kHz 2 mN 200 kHz Linear
Pressure measurements	p	**Pressure scanner** *Scanivalve MPS4264*	Full-scale range Accuracy/Resolution Dynamic response	$\pm$ 1000 Pa $\pm 0.15\%$ FS $= \pm 1.5$ Pa 850 Hz

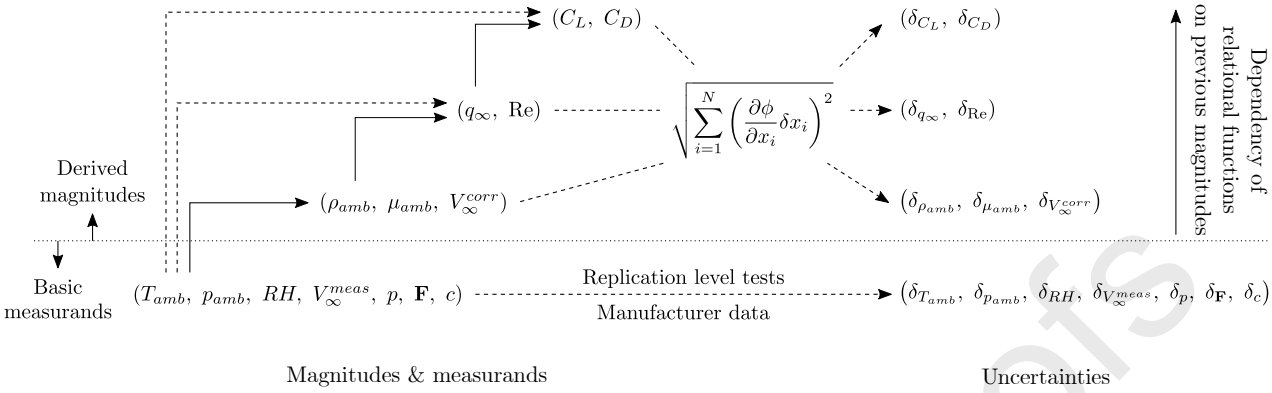

Figure 2: hierarchical structure resultant from the functional relation of derived magnitudes with respect to either basic measurands or other derived magnitudes, and the uncertainty analysis to be performed at each level. Notice that the hierarchy is based on the degree of dependency of the functional relations of the variables on previous magnitudes. Those directly related to basic measurands lie at lower hierarchical levels, whereas the ones depending on both basic measurands and other derived magnitudes occupy higher positions.

This method is based on traversing a wake-rake device behind the airfoil for measuring the momentum deficit introduced by it, and obtaining the drag coefficient by integrating such a profile. The wake-rake device consists of a comb-like array of 18 total head probes covering a dimension of nearly 50 mm, which amounts to a third of the airfoil's chord. The referential pressure is measured at the floor of the tunnel, which equals the static pressure at the station of the wake-rake device and turns the total head measurements into dynamic heads. The wake-rake device is attached to a 3D-axis positioning system driven by three stepper motors, allowing its motion throughout the tunnel and, specifically, enabling the transversal surveys behind the airfoil. Additionally, a fourth stepper motor is located on a sealed box underneath the central panel of the tunnel, driving a rotary plate around a constant vertical axis.

The piezoelectric balance is fixed to this plate, and the airfoil gets attached to it by means of an auxiliary rod. Thus, the action of the fourth stepper motor causes the variation of the angle of attack of the airfoil, which permits to obtain the characteristic lift and drag curves. The Pitot-static probe, used to measure the inflow velocity, is located at the entrance of the test-section, while the ambient conditions transmitter monitorizes the ambient parameters from the outside. Together, they provide the means for controlling the airfoil's chord based Reynolds number.

In order to ensure that relevant statistics of lift and drag signals are computable from the output data, 5-seconds-long measurements are performed at each of the angular configurations. Although a single measurement suffices for obtaining a lift signal, the momentum deficit method requires splitting the transversal survey into seven non-overlapping sections for capturing the wake acceptably. This is so because the wake-rake device is located 2.5 chord distances downstream the airfoil due to the physical restriction imposed by the end plates. The purpose of such ennd plates is to ensure that a two-dimensional flow is obtained in the test-section, and are located leaving a gap of 2 mm at the floor and ceiling of the tunnel. This downstream distance is assumed to be acceptable according to [13, 14]. Anyhow, this protocol makes the testing of a single drag curve to take as long as an hour, in comparison to the 10-minutes-long lift-curve testing. Typical airfoil-testing surveys, besides, require computing several lift and drag curves, either for a set of different configurations (i.e. distinct Reynolds numbers) or by running a number of tests for the same configuration in order to ensure repeatability. In any case, it is common to have the tunnel working for periods of several hours. The replication levels philosophy is to be applied on this characteristic time-lapse for obtaining relevant uncertainty intervals.

As stated in Section 2, the replication level tests are applied to the set of basic measurands. The 0^{th} order replication level is reproduced with the aim of calculating the influence of possible electrical circuitry flaws and potential equilibrium thermodynamic fluctuations on the measurements. Electrical circuitry related

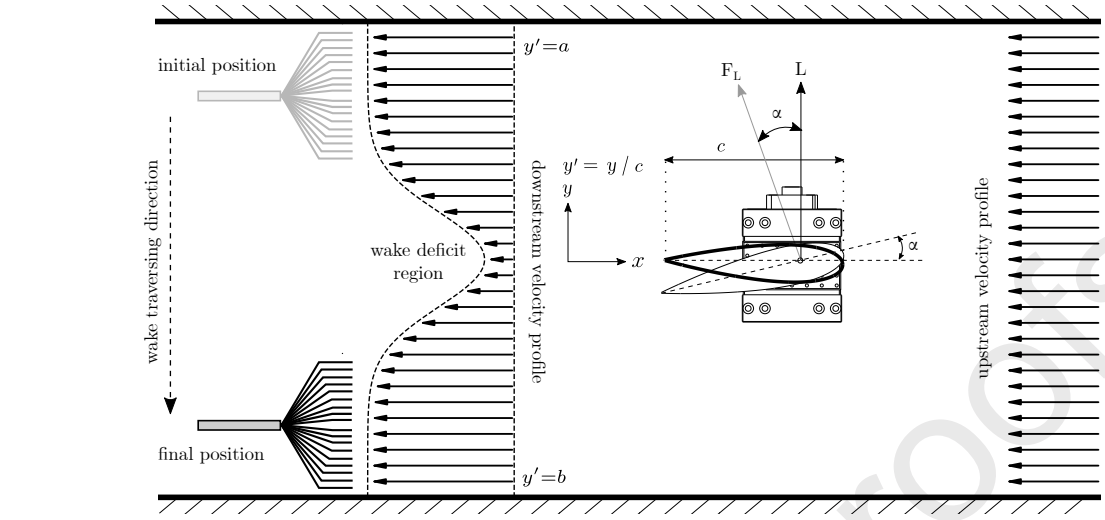

(a) schematic drawing of the experimental methods employed for obtaining C_L and C_D coefficients.

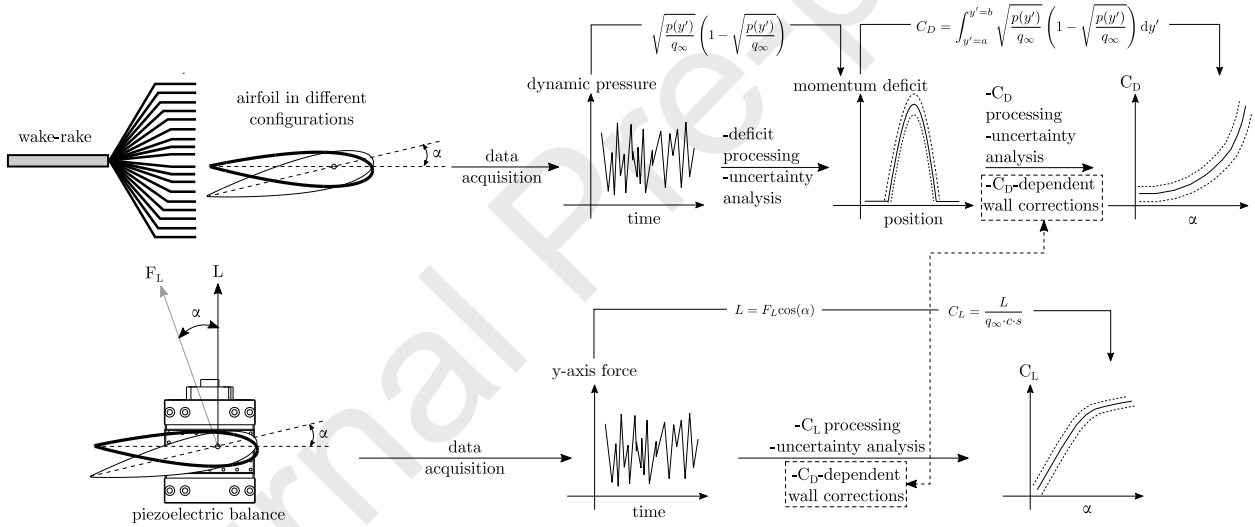

(b) workflows showing the sequential stages for calculating C_L and C_D coefficients parting from the data acquisition operation.

Figure 3: conceptual representation of the overall experimental workflow followed for calculating C_D and C_L coefficients. Figure 3a is a schematical drawing of the experimental set-up on a generic measurement configuration; Figure 3b intends to illustrate the post-processing steps for obtaining the coefficients.

perturbations are assessed by disconnecting the probe-side end of the devices and letting the signal travel back to the acquisition system, in order to detect deviations lying above the resolution level of the devices. Equilibrium thermodynamic fluctuations are addressed by connecting the probe-side ends and performing the measurements with the tunnel being inoperative.

Measurements regarding the 1^{st} order replication level are intended to quantify the timewise jitter on the output signals and, consequently, the tunnel must be operative. Additionally, certain measurements need baseline cases for comparing the output data to expected values in order to compute the jitter adequately: it is the case of the piezoelectric balance and the pressure scanner. The baseline case used for the piezoelectric balance is the 0° angle-of-attack configuration of the airfoil, which theoretically provides a null lift output;

the airfoil is aligned prior to the 1^{st} order replication level test so that a proper $0°$ configuration is set. The baseline case for the pressure scanner is obtained by placing a flat plate perpendicular to the incoming flow and practicing orifices for measuring the correspondent total head. When the plate is perpendicularly aligned with the flow and the reference pressure of the scanner is taken from the outside, the total head ports provide the pressure losses introduced by the elements of the tunnel placed before the test-section, which are characterized in [15].
The uncertainty intervals coming from possible calibration errors are estimated from the specification sheets of the devices, interpreting the calibration error data as standard deviations obtained with a 95% confidence level.
The chosen characteristic time-lapse for performing the 0^{th} and 1^{st} order replication level tests is of 5 hours, with 5-seconds-long measurements being taken each 6 minutes (10 measurements per hour). The ambient conditions transmitter and the Pitot-static probe are set to their maximum sampling frequency rates, which is of 20 Hz for both devices. The piezoelectric balance is subjected to a rate-dependency test. According to [16], consistent sampling frequencies are those for which the averages of the output signals reach constant values. In other words, it is to be assessed that those values do not depend on the chosen sampling frequency. The rate-dependency test as proposed by [16] yields a minimum sampling rate of 500 Hz for the balance, considered to be high enough as to resolve the airflow-airfoil interactions of interest. Additionally, the balance is known to show a linear electrical drift on the output signals due to the inherent activity of the piezoelectric crystals. This drift is compensated by taking initial and final measurements with the tunnel being inoperative, and substracting the correspondent linear portion to the measurements taken in between. Lastly, the pressure scanner's rate is set to its maximum value of 850 Hz.

4. Results and discussion

The former part of this section is concerned with the uncertainty analysis of the set of basic measurands, obtained by applying the replication levels philosophy as stated in Sections 2 and 3. The second part consists of a combined approach: it exposes how the uncertainty intervals of basic measurands are propagated to derived magnitudes, and shows the influence of the operative conditions on the physical magnitudes due to large tunnel operation periods.

4.1. Uncertainty analysis of basic measurands

Table 2 shows, with the set of devices ordered as in Table 1, the computed uncertainty intervals for each of the replication levels. It is to notice that the quantities represent full-scale percentages, so that the relative importance of the perturbations that affect each of the devices are normalized on a common basis. The contributions of the perturbations are considered negligible if they fall below 10^{-3}% of the full-scale output, as they do not change the overall uncertainty value appreciably in those cases; mind, besides, that this overall uncertainty comes from applying Equation (2) to the uncertainty terms that do not happen to be negligible. The relevant remarks to be made are:

- the noticeably high calibration errors of T_{amb}, RH and V_∞, which largely overcome the timewise jitter contributions and make the overall uncertainty depend mainly on a proper calibration of the correspondent sensors.

- The non-negligible 0^{th} order contributions of the piezoelectric balance. These contributions stem from the fact that the inherently small output signals of the balance need to be augmented by an intermediate amplifier. This amplifier introduces an appreciable white noise in the signal even for the inoperative tunnel conditions. Notice, additionally, that the timewise jitters are identical for the three axes. This is so because, as stated in Section 3, the only baseline case for computing the jitter is the null lift force obtained for the $0°$ angle-of-attack configuration of the airfoil. Such a baseline case merely allows determining the F_y-related jitter, and the assumption is made that the other two axes show the same scattering.

Table 2: uncertainty table of the analysed probes (units in % full-scale of each device).

Device/variable		0^{th} **order**	1^{st} **order**			N^{th} **order**
			System perturbations, System/sensor interactions	**Timewise jitter**	**Calibration error**	**Overall uncertainty**
Ambient conditions transmitter	p_{amb}	negligible	negligible	$4.76{\cdot}10^{-3}$	$1.81{\cdot}10^{-2}$	$\sqrt{(4.76{\cdot}10^{-3})^2 + (1.81{\cdot}10^{-2})^2} = 5.09{\cdot}10^{-2}$
	RH			$2.38{\cdot}10^{-2}$	1.4	$\sqrt{(2.38{\cdot}10^{-2})^2 + 1.4^2} = 1.4$
	T_{amb}				0.15	$\sqrt{(2.38{\cdot}10^{-2})^2 + 0.15^2} = 0.152$
Pitot-static probe	V_∞	negligible	negligible	$3.83{\cdot}10^{-2}$	0.958	$\sqrt{(3.83{\cdot}10^{-2})^2 + 0.958^2} = 0.959$
Piezoelectric balance	F_x	$5.08{\cdot}10^{-2}$	Configuration-dependent[8], $\delta F_{conf.}$	0.44	-0.375	$^{(9)}sgn(x)\sqrt{\lvert(\delta F_{x_{conf.}})^2 + 0.44^2 - (0.375)^2\rvert}$
	F_y	$5.06{\cdot}10^{-2}$			-0.418	$sgn(y)\sqrt{\lvert(\delta F_{y_{conf.}})^2 + 0.44^2 - (0.418)^2\rvert}$
	F_z	$2.84{\cdot}10^{-2}$			-0.589	$sgn(z)\sqrt{\lvert(\delta F_{z_{conf.}})^2 + 0.44^2 - (0.589)^2\rvert}$
Pressure scanner	p	negligible	Configuration-dependent[10], $\delta p_{conf.}$	$7.5{\cdot}10^{-2}$	negligible	$\sqrt{(\delta p_{conf.})^2 + (7.5{\cdot}10^{-2})^2}$

(8) *ad hoc* tests for assessing wall and support interferences.
(9) calibration terms remain negative to account for the bias; sign functions (sgn) equal the sign of the overall terms inside the roots.
(10) *ad hoc* tests for assessing systematic errors on static or total heads, whichever it is to be measured.

- The configuration-dependent perturbations that are left undetermined for the piezoelectric balance ($\delta F_{conf.}$) and the pressure scanner ($\delta p_{conf.}$). These are to be specified for each of the particular experimental layouts being tested. Techniques for treating support interferences that affect load measurements are to be found in [17, 18], whereas correction factors for pressure taps measurements (either total or static) are reported in [19]. For the tests assessing replication level uncertainties, it suffices to say that the configuration-dependent perturbations are found to be negligible when compared to the other contributions.

- According to the manufacturer's specifications, the calibration errors of the piezoelectric balance have a negative sign and do not comply with the typical $\pm$ convention. This turns necessary the introduction of the sign function ($sgn(x)$) on the computation of the overall uncertainty, which takes the sign of term resulting from the combined operation performed with the members within the root.

4.2. Effect of operative conditions and propagation of uncertainties to derived magnitudes

In order to follow a structured narrative, the influence of the operative conditions is first discussed on a general basis. The combined effect of these operative conditions and the basic measurand uncertainties computed in Section 4.1 are addressed on the set of derived magnitudes secondly.

4.2.1. Effect of operative conditions

The 5-hours-long test for assessing 1^{st} order replication level uncertainties shows that the tunnel is prone to introduce severe changes on the ambient conditions, as observed in Figure 4. Notice that the employed

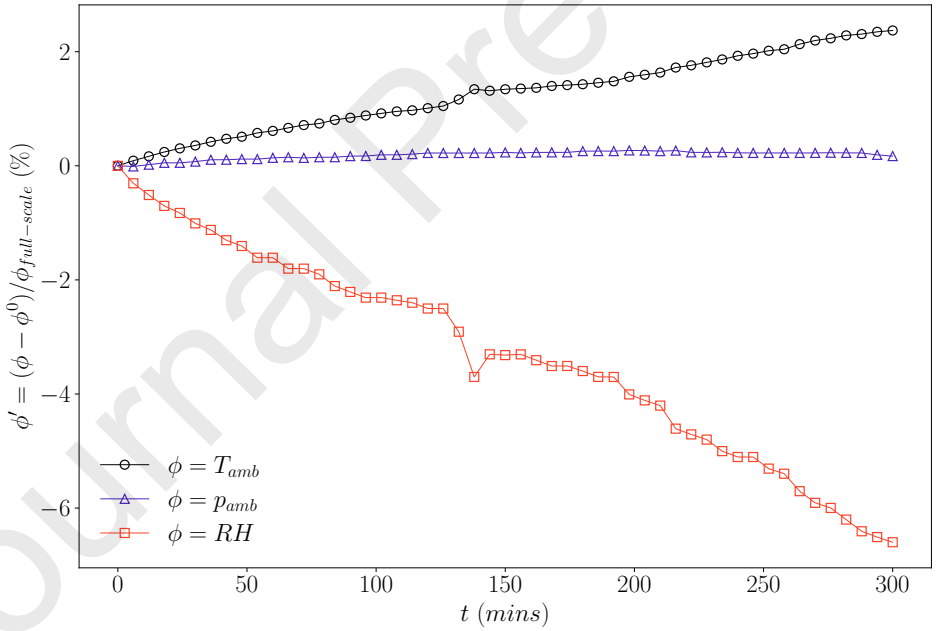

Figure 4: temporal evolution of the ambient condition parameters, namely T_{amb}, p_{amb} and RH, due to the changes introduced by the operative conditions of the tunnel. Notice the y-scale employed, which provides the relative difference of each magnitude with respect to initial conditions normalized with the correspondent full-scale value.

y-scale represents the relative difference of each magnitude with respect to initial conditions, normalized with the correspondent full-scale value.
Seemingly, temperature and relative humidity get noticeably affected by the tunnel's work, with the airflow becoming hotter and drier during the test. The physical mechanism behind this behaviour is to be found on the heat losses stemming from the tunnel's power source. Those heat losses get propagated to the overall

room due to convection, mainly because of the open circuit design of the tunnel. The evolutions are observed to cause changes that amount to nearly 3% and 7% in T_{amb} and RH respectively, which according to Table 2 correspond, on dimensional grounds, to variations of 3°C and 7%.
The ambient pressure, as expected, is not affected by changes on the airflow conditions. Although differences with initial conditions do not remain constant, the deviations from a null value are small enough as to assume constancy, and do not show as clear a trend as the other two magnitudes. These erratic changes are ascribed to natural variations in p_{amb} during daytime.
It is to recall that the curves in Figure 4 represent variations corresponding to a specific test, and that they may change quantitatively depending on factors such as the testing day, the time of the day at which the testing begins or the testing plan itself. However, it has been assured that the qualitative character of the curves is independent of any external factor. In other words, it has been assessed that the tunnel's work causes an increase in temperature and a decrease in humidity regardless of the testing day, and that the ambient pressure is unaffected accordingly. Additionally, information regarding the uncertainty intervals of the represented magnitudes is absent in Figure 4, as these intervals are to be discussed together with their propagation to the derived magnitudes in what follows.

4.2.2. Propagation of uncertainties to derived magnitudes

The upcoming discussion is ordered following a simplicity criterion on the functional dependency of the derived magnitudes. The magnitudes most directly related to the set of basic measurands are presented first, with the ones owning the simplest functional relations leading the classification. Magnitudes that partly depend on basic measurands, and partly on other derived magnitudes, are addressed next, considering the same simplicity criterion as for the former ones.

- Corrected velocity, V_∞^{corr}: regarding the manufacturer's specifications, the full-scale (and, consequently, the measured velocity) of the Pitot-static probe depends on both T_{amb} and p_{amb} in a linear fasion. Figure 5 intends to show how such a dependency affects the corrected value, and is to be read together with the V_∞^{corr}-related data in Table 3. The figure represents, scaled on its left-hand side y-axis, the variations in T_{amb} and p_{amb} already depicted in Figure 4, but with the additional information of their respective uncertainty intervals rendered as hatched regions around the mean values. Notice that, although the uncertainty interval of T_{amb} is clearly noticeable, that of p_{amb} happens to show a marginal influence on the corresponding dataset, agreeing with the values shown in Table 2.
  The velocity-related data is represented, on the right-hand side y-axis, in two different series. Notice that the employed scale represents corrected velocity fluctuations normalized with the full-scale velocity. However, those fluctuations are represented as depending on a generic argument ψ that is different for each of the series. The bottom curve ($\psi = V_\infty^{corr}$) represents the variation of the corrected velocity with respect to the initial corrected velocity, which is why it begins the temporal evolution from a null value. The upper one shows the difference between the corrected and the initial measured velocities ($\psi = V_\infty^{meas}$). Its upwards shift with respect to the former curve is to be ascribed, obviously, to the effect of the correction. Notice, additionally, that the velocity curves are evidently modulated by the temperature signal, with the characteristic central peak being discernible in both of them. If the row corresponding to V_∞^{corr} is read from Table 3, it is observed that the factors entering the uncertainty expression (Equation (2)) are the uncorrected velocity (V_∞^{meas}) and the ambient temperature and pressure (T_{amb} and p_{amb}). Such an expression entails a root operation of the sum of the squared terms. It is not possible, hence, to derive the exact contribution of each of the terms to the overall uncertainty. However, squaring Equation (2) provides the following expression:

$$\delta^2 = \sum_{i=1}^{i=N} \left(\frac{\partial \phi}{\partial x_i} \delta_{x_i} \right)^2, \tag{3}$$

  which shows that it is possible to estimate the contribution of a particular magnitude x_i thusly:

$$\text{Relative contribution (\%) of } x_i = \left(\frac{\partial \phi}{\partial x_i} \delta_{x_i} \right)^2 / \delta^2. \tag{4}$$

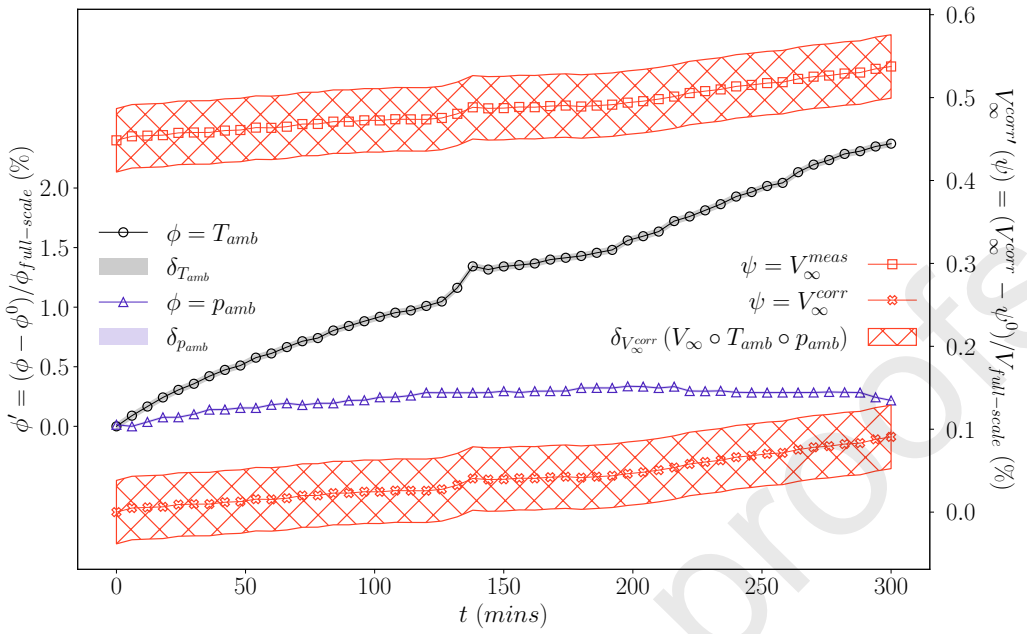

Figure 5: temporal evolution of the corrected velocity, relative to its initial value and to the measured value (left hand-side y-axis), together with the evolutions of T_{amb} and p_{amb}(right hand-side y-axis). The hatched regions correspond to the uncertainty intervals of each of the depicted curves. Notice the y-scale employed, which provides the relative difference of each magnitude with respect to the initial conditions normalized with the correspondent full-scale value.

The row corresponding to V_∞^{corr} shows that the contributions of T_{amb} and p_{amb} to the overall uncertainty of the corrected velocity are negligible when compared to the uncertainty interval of V_∞^{corr}. This indicates that T_{amb} and p_{amb} variations influence the uncertainty interval of V_∞^{corr} in three ways. Firstly, via the partial factor $\partial V_\infty^{corr}/\partial V_\infty^{meas}$. Secondly, by introducing a bias error of approximately 0.45% of the full-scale value on the measured velocity. Lastly, by partially modulating the evolution of the corrected velocity (it increases nearly 0.1% of the full-scale value). Certainly, though, the scattering of V_∞^{corr} is mainly due to the uncertainty interval of V_∞^{meas}, whose propagation to the corrected velocity gets reflected on the hatched regions of the figure.

- Air density and viscosity, ρ_{amb} and μ_{amb}: a similar analysis as for the corrected velocity may be performed on the basis of Figure 6.
  In order to avoid excessive chartjunk, the curves corresponding to basic measurands are omitted, keeping merely the ones corresponding to ρ_{amb} and μ_{amb}. Additionally, mind that the scaling on both y-axes is not performed with a full-scale normalization, as it is not possible to define such a quantity for these derived magnitudes. Instead, the normalizing factors are the initial values of the magnitudes. It is observed that the temporal evolutions of both magnitudes are severely modulated by temperature and humidity signals, even more so than in the case of the corrected velocity. The sustained variations are also larger, approaching a value of 1% in both cases, as opposed to the 0.1% change on V_∞^{corr}. The double hatched regions in both curves are meant to illustrate, qualitatively, the data represented in the corresponding rows of Table 3. It is to notice that the relative humidity factor is the main contributor of the uncertainty intervals, with a major effect on $\delta_{\rho_{amb}}$. Although the largest regions include the influence of the triplet (RH, T_{amb}, p_{amb}) on the intervals, it is to mention that the pressure factor is either marginal or negligible, and that the contributions of RH and T_{amb} come from the higher uncertainties that those measurands own by default (see Table 2).

- Upstream dynamic pressure and Reynolds number, q_∞ and Re: for the sake of illustrative cleanness, and as both magnitudes happen to show quantitatively similar trends, Figure 7 merely represents the

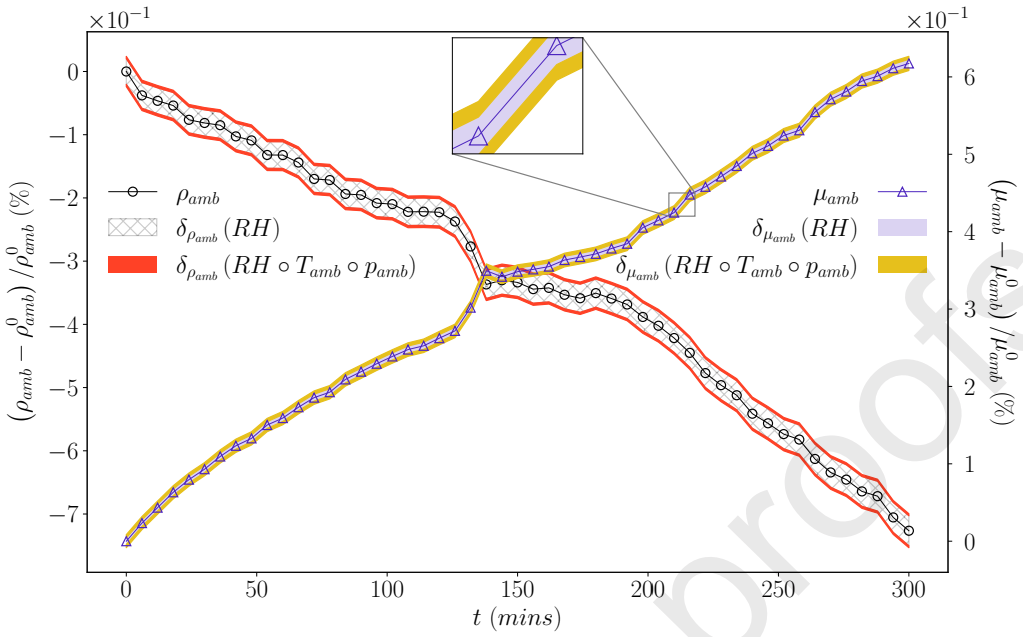

Figure 6: temporal evolution of ambient density (left hand-side y-axis) and viscosity (right hand-side y-axis). The overlapped hatched regions are meant to represent the contributions of different factors to the overall uncertainty, and are ordered so that the largeset contributor's region is placed around the average curve, with smaller contributors' regions wrapping that central band. Series are scaled by substracting the correspondent initial values to the datasets, and normalizing with those values.

Reynolds number's evolution. Thus, the characteristic lift and drag curves that are shown further on, obtained for both constant and changing Reynolds numbers, may be understood on the basis of the following graphical example. The y-axis scaling is performed as in Figure 6.
The opposite evolutions of ρ_{amb} and μ_{amb}, and their higher variation rates in comparison to V_∞^{corr}, cause a sustained Reynolds number diminution during the test, which is also clearly modulated by temperature and humidity signals. The continuous decrease in the average values, which grows as large as 1.5% at the end of the test, overcomes the computed uncertainty interval ($\approx 0.4\%$) in a 30-minutes lapse. The major contributor is the corrected velocity's uncertainty, with density showing a marginal influence and viscosity and the length-dependent factors being negligible (see Table 3). The length-dependent factor (i.e. relative to the airfoil's chord) is obtained by setting the δc value to the average roughness on the chordwise dimension, which is of 1.4 μm.
The analysis above is equally applicable to the upstream dynamic pressure magnitude, q_∞, with V_∞^{corr} being the main contributor to the uncertainty and density being marginal. Otherwise, the extent of the uncertainty region and the variation of the average values follow quantitatively similar trends as for the Reynolds number.

- Momentum-deficit-computed drag coefficient, C_D: the wake-rake methodology described in Section 3, when applied to the present case-study, provides an unfiltered momentum deficit curve as the one represented by the triangular symbols in Figure 8. Theoretically, the momentum deficit expression should reach a null value outside the wake, but perturbations in the flowfield and measurement uncertainties cause the observed scattering on the data. It is evident that integrating this raw data leads to spurious C_D values, as the contribution of the scattering to the integration may not be null or negligible. It turns necessary, hence, to filter the curve so that the points outside the wake are set to their expected null values. This poses the problem of delimiting the wake somehow, by imposing a suitable threshold value that leaves the spurious points outside. Such a threshold is set to the momentum-deficit value corresponding to the q_∞ uncertainty. Beginning from the wake's peak, which is unambiguously

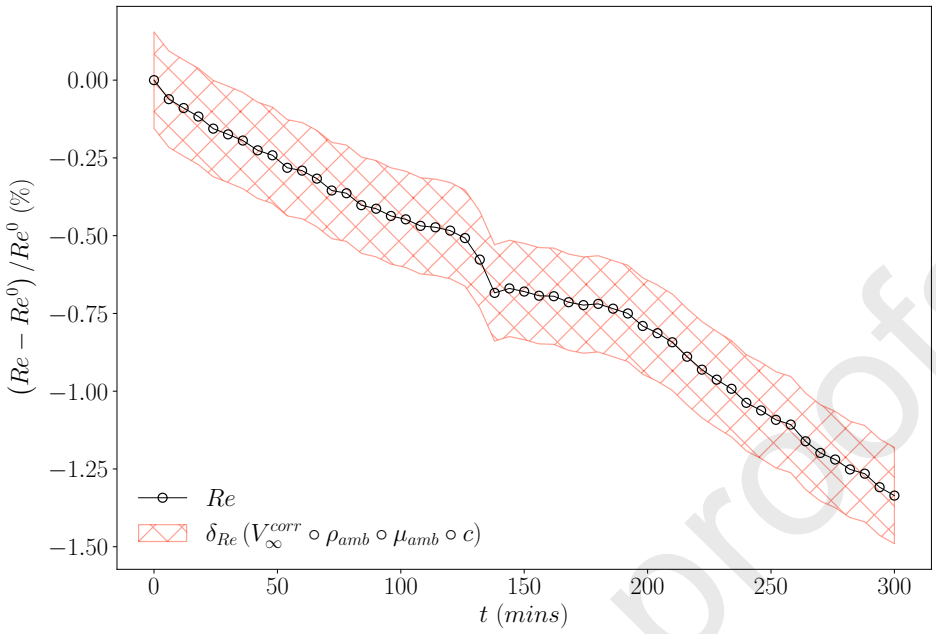

Figure 7: temporal evolution of Reynolds number. The hatched region represents the contributions to the overall uncertainty. Data is scaled by substracting the initial value to the overall set, and normalizing with that initial value.

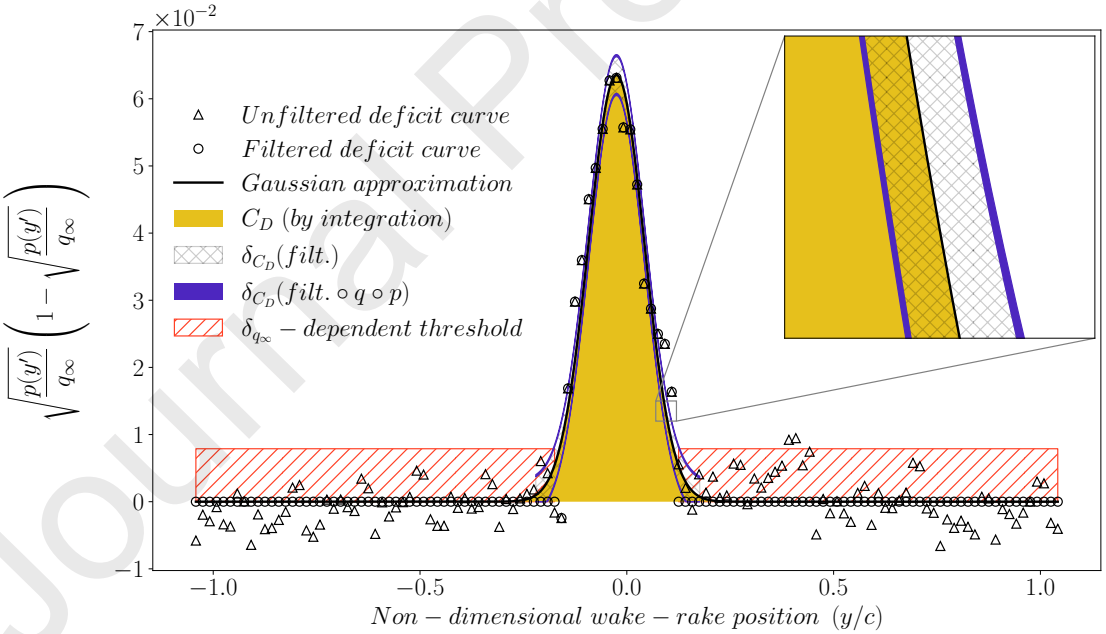

Figure 8: unfiltered and filtered momentum-deficit curves for a given angular configuration of the NACA0021 airfoil. The triangular symbols represent the unfiltered deficit curve, whereas the dots come from applying the filtering process. The approximate gaussian curve is meant to illustrate the bell-shaped character of the wake's energetic profile, and to ease the depiction of the uncertainty regions. Those regions are hatched differently depending on the factors that contribute to the uncertainty.

identifiable, the delimiting process goes through both halves of the curve, and the first points lying below the threshold are considered as the edges of the wake. Further points are consequently set to null values, with the resultant filtered curve being represented by black dots in Figure 8. This filtering unavoidably introduces an uncertainty $\delta filt$ corresponding to the points excluded from the integration process, which is obtained by computing the standard deviation of the original values of those points. Additionally, the points of the wake are subjected to the combined uncertainty intervals of pressure measurements and q_∞. The gaussian approximation of the wake, represented by the black line in Figure 8, is meant to illustrate its shape, and to facilitate the drawing of the different contributions to the uncertainty interval. Data in Table 3 shows that the governing factor is the filtering process, with q_∞ having a slight influence and pressure measurements owning a negligible effect.
Notice, lastly, that the expression for the overall uncertainty value shown in Table 3 does not comply with Equation (2) in this case. As the hatched regions representing the deficit curve uncertainties are to be integrated for obtaining a C_D value, maximum and minimum integrands correspond to the highest and lowest curves. The contribution of a particular factor, hence, is merely the area of its hatched region, and the overall uncertainty is obtained by simply adding the different contributions.

- Corrected lift and drag coefficients, C_L^{corr} and C_D^{corr}: Figure 9 represents the lift and drag curves of the NACA0021 airfoil obtained for a nominal Reynolds number of 10^5 and for angles of attack spanning the range $0-12°$. Both left- and right-hand side y-axes represent the corrected non-dimensional coefficients, with the corrections addressing tunnel wall interferences, as described in [12]. The uncorrected datasets are not represented in the figure, but it is worth saying that, for the relatively low angles of attack considered, the blockage effect of the airfoil shows an almost negligible effect, and that the corrected dataset collapses into the uncorrected one. Nevertheless, the correction is applied as part of the post-processing protocol. Notice, besides, that there are two x-axes on the figure. The bottom one

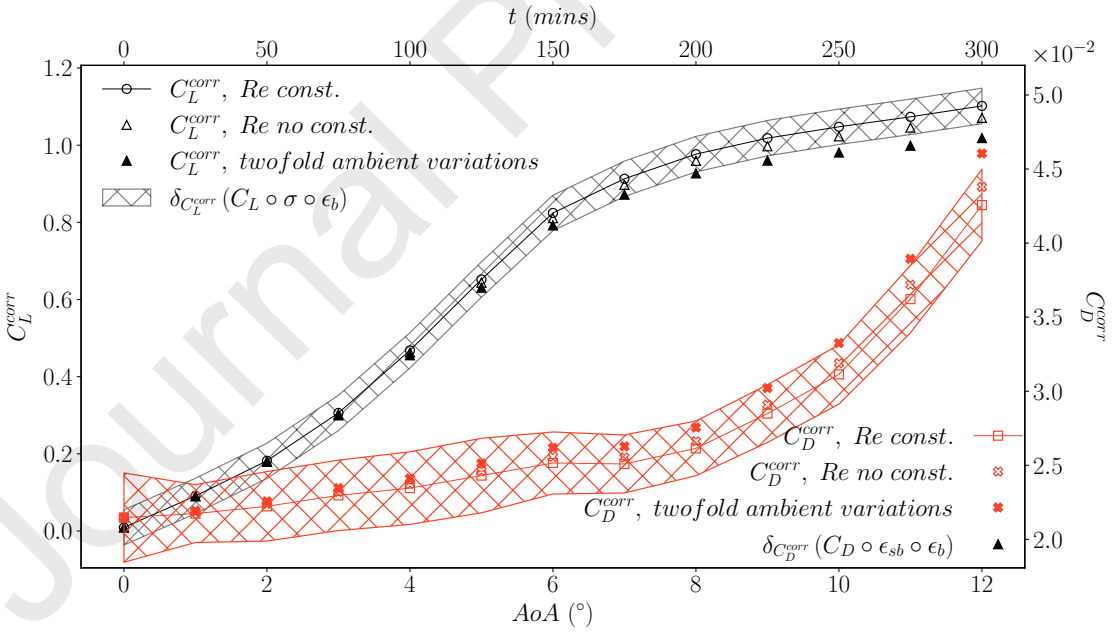

Figure 9: characteristic lift and drag curves (left and right hand-side y-axes, respectively) for the NACA0021 airfoil in a Re=10^5 configuration, obtained by temporally equispaced measurements along a 5-hours-long operative lapse. Notice that there are two x-axes as well. The bottom one represents the angular configuration of the airfoil, whereas the upper one is a temporal axis.

represents the angular configuration of the airfoil; the upper one, instead, is a temporal axis. In order to show how the varying operative conditions may affect the curves, the datasets are obtained by

performing temporally equispaced measurements along a 5-hours-long operative lapse. Thus, they comply with the same conditions under which the replication level tests are undertaken. This means that a measurement is performed every 25 minutes, as observed in the top x-axis.

Each coefficient owns three different datasets, which are obtained in nominally identical configurations, but considering distinct guidelines regarding the operative conditions control. In the light of Figure 7, keeping a constant Reynolds number requires increasing the testing velocity progressively, so that the resultant evolution curve becomes a straight horizontal line fixed at a predefined value. Thus, the datasets claimed to be obtained under constant Reynolds number conditions fulfill the mentioned specification. For the remaining ones, instead, it is assumed that the Reynolds number is varying.

The curves under the denomination of non-constant Reynolds number are obtained by considering that the Reynolds variation happens as shown in Figure 7. Increasing the velocity for compensating the diminution of the Reynolds number due to operative conditions has a number of consequences. The straightforward one is that the q_∞ value also increases, as it is squarely proportional to the testing velocity. As additional side effects, higher velocities may also cause changes on the loads acting on the airfoil, and variations in the pressure measurements implied in the wake-rake method. However, these are found to be small in comparison to the q_∞ variation, which affects the computation of both C_L and C_D coefficients. The C_L coefficient gets influenced via the non-dimensionalizing factor, and the C_D one because of its presence in the momentum-deficit expression. Both coefficients, besides, show a drifting behaviour as the tesing time proceeds. However, such a drift does not cause the uncontrolled coefficients to fall outside the estimated experimental uncertainty, although the latest measurement points do lie close to the edges of the intervals. A conclusion may be drawn, thus, that controlling the operative conditions is not as critical as the temporal evolutions of certain magnitudes suggest.

Nevertheless, it is to notice that such temporal variations may become harsher under circumstances other than the ones employed herein. Mind that, as mentioned before, the changes in T_{amb} and RH are dependent on factors such as the testing plan or testing day. Regarding the testing plan, it is to mention that the undertaken tests are performed by setting a nominally constant inlet Reynolds number of 10^5. Typical air density and viscosity values, together with the airfoil's chord c, yield an inlet velocity of ≈ 10 m/s for achieving such a Reynolds number. However, the transitional regime of interest may extend up to Reynolds numbers of $5{\cdot}10^5$ [20], which require higher inlet velocities. This increase, in turn, causes major power losses due to the cubically proportional relation between both magnitudes, $P \propto V_\infty^3$. Additionally, higher velocities enhance the mixing mechanism via convection, thus promoting steeper evolutions of temperature and humidity within the room. Anyhow, lift and drag coefficient curves obtained under such circumstances would not be comparable to the ones shown in Figure 9 due to the different fluid configurations, which are highly dependent on the Reynolds number in the transitional regime. The point to make, besides, is that tests performed under higher Reynolds numbers are prone to show variations in ambient conditions that, if uncontrolled, may deviate lift and drag coefficients outside their respective experimental uncertainty regions.

A different scenario arises when considering the possible influence of external factors, such as changes in environmental conditions during the testing day. The third set of curves in Figure 9, represented by the filled symbols, are obtained by considering the hypothesis that the temporal evolutions of the ambient conditions are twice as greater as the ones shown in Figure 4, a highly plausible fact considering the daily temperature and humidity evolutions registered in the room. As for the second datasets commented before, these curves are also computed by assuming that no control is set on the monitoring process of the ambient conditions. The results are revealing insofar they highlight two relevant factors: the first is that there exist critical evolutions of the ambient conditions beyond which the environmental changes are capable of introducing errors in the measurements such that the resultant deviations lie outside the estimated experimental uncertainty. The second is the non-linear relationship between those deviations and the temporal evolutions that produce them. When comparing the twofold evolution case with the nominal one, it is observed that the latter introduces errors slightly above 2% in the average values of C_L and C_D, whereas the former increases those errors up to 8%. Besides, notice that the temporal lapse required for producing experimentally mislead measurements is larger than 200 minutes. However, the claim made herein is not that a proper control is

unneccesary unless the overall testing survey lasts longer than the mentioned period. Instead, the point to make is that the estimated true values get noticeably affected if changes on environmental conditions are not taken into account, up to the point of turning those values experimentally unacceptable. Obviously, the task of determining the critical conditions and time-lapses for which this phenomenon happens is purely configuration-dependent, and an issue that the experimentalist is forced to consider at the designing stage of experimental tests.

Finally, mind that the main contributions to the intervals come from the uncorrected coefficients themselves (see Table 3), which means that the correction factors do not do not affect those intervals. The major influences on C_D have already been discussed, concluding that the filtering uncertainty, $\delta_{filt.}$, is directly propagated into the C_D^{corr} interval. Besides, the lift force factor δ_{F_L} is the only contributor to the C_L uncertainty range, and consequently to the C_L^{corr} one. Hence, the q_∞ variable does not determine the computed intervals, but it causes the deviations on the average values if the operative conditions are not controlled.

Table 3: functional relations, partial contributions and overall uncertainty intervals of derived magnitudes.

Magnitude	**Relational function**	**Partial expressions**	**Relative contributions (%)**	**Overall δ expression**	**Average δ value**
V_∞^{corr} (m/s)	$f\left(V_\infty^{meas}, T_{amb}, p_{amb}\right)$	$\frac{\partial V_\infty^{corr}}{\partial V_\infty^{meas}}\delta V_\infty^{meas}$	100	$\left[\left(\frac{\partial V_\infty^{corr}}{\partial V_\infty^{meas}}\delta V_\infty^{meas}\right)^2 + \right.$	$1.58{\cdot}10^{-2}$
		$\frac{\partial V_\infty^{corr}}{\partial T_{amb}}\delta T_{amb}$	negligible	$+\left(\frac{\partial V_\infty^{corr}}{\partial T_{amb}}\delta T_{amb}\right)^2 +$	
		$\frac{\partial V_\infty^{corr}}{\partial p_{amb}}\delta p_{amb}$	negligible	$\left. + \left(\frac{\partial V_\infty^{corr}}{\partial p_{amb}}\delta p_{amb}\right)^2\right]^{1/2}$	
ρ_{amb} (kg/m^3)	$f\left(T_{amb}, RH, p_{amb}\right)$	$\frac{\partial \rho_{amb}}{\partial T_{amb}}\delta T_{amb}$	12	$\left[\left(\frac{\partial \rho_{amb}}{\partial T_{amb}}\delta T_{amb}\right)^2 + \right.$	$3{\cdot}10^{-4}$
		$\frac{\partial \rho_{amb}}{\partial RH}\delta RH$	87	$+\left(\frac{\partial \rho_{amb}}{\partial RH}\delta RH\right)^2 +$	
		$\frac{\partial \rho_{amb}}{\partial p_{amb}}\delta p_{amb}$	1	$\left. + \left(\frac{\partial \rho_{amb}}{\partial p_{amb}}\delta p_{amb}\right)^2\right]^{1/2}$	
μ_{amb} (kg/(m·s))	$f\left(T_{amb}, RH, p_{amb}\right)$	$\frac{\partial \mu_{amb}}{\partial T_{amb}}\delta T_{amb}$	46	$\left[\left(\frac{\partial \mu_{amb}}{\partial T_{amb}}\delta T_{amb}\right)^2 + \right.$	$1.6{\cdot}10^{-9}$
		$\frac{\partial \mu_{amb}}{\partial RH}\delta RH$	54	$+\left(\frac{\partial \mu_{amb}}{\partial RH}\delta RH\right)^2 +$	
		$\frac{\partial \mu_{amb}}{\partial p_{amb}}\delta p_{amb}$	negligible	$\left. + \left(\frac{\partial \mu_{amb}}{\partial p_{amb}}\delta p_{amb}\right)^2\right]^{1/2}$	

Table 3: continued.

Magnitude	Relational function	Partial expressions	Relative contributions (%)	Overall δ expression	Average δ value
q_∞ (Pa)	$f\left(\rho_{amb}, V_\infty^{corr}\right)$	$\frac{\partial q_\infty}{\partial \rho_{amb}}\delta\rho_{amb}$	1	$\left[\left(\frac{\partial q_\infty}{\partial \rho_{amb}}\delta\rho_{amb}\right)^2 + \right.$	0.26
		$\frac{\partial q_\infty}{\partial V_\infty^{corr}}\delta V_\infty^{corr}$	99	$\left.+\left(\frac{\partial q_\infty}{\partial V_\infty^{corr}}\delta V_\infty^{corr}\right)^2\right]^{1/2}$	
Re (−)	$f\left(\rho_{amb}, V_\infty^{corr}, \mu_{amb}, c\right)$	$\frac{\partial \mathrm{Re}}{\partial \rho_{amb}}\delta\rho_{amb}$	2	$\left[\left(\frac{\partial \mathrm{Re}}{\partial \rho_{amb}}\delta\rho_{amb}\right)^2 + \right.$	1647
		$\frac{\partial \mathrm{Re}}{\partial V_\infty^{corr}}\delta V_\infty^{corr}$	98	$+\left(\frac{\partial \mathrm{Re}}{\partial V_\infty^{corr}}\delta V_\infty^{corr}\right)^2 +$	
		$\frac{\partial \mathrm{Re}}{\partial \mu_{amb}}\delta\mu_{amb}$	negligible	$+\left(\frac{\partial \mathrm{Re}}{\partial \mu_{amb}}\delta\mu_{amb}\right)^2 +$	
		$\frac{\partial \mathrm{Re}}{\partial c}\delta c$	negligible	$\left.+\left(\frac{\partial \mathrm{Re}}{\partial c}\delta c\right)^2\right]^{1/2}$	
C_L (−)	$f\left(F_L, q_\infty, A\right)$	$\frac{\partial C_L}{\partial F_L}\delta F_L$	100	$\left[\left(\frac{\partial C_L}{\partial F_L}\delta F_L\right)^2 + \right.$	$4.67{\cdot}10^{-2}$
		$\frac{\partial C_L}{\partial q_\infty}\delta q_\infty$	negligible	$+\left(\frac{\partial C_L}{\partial q_\infty}\delta q_\infty\right)^2 +$	
		$\frac{\partial C_L}{\partial A}\delta A$	negligible	$\left.+\left(\frac{\partial C_L}{\partial A}\delta A\right)^2\right]^{1/2}$	

Table 3: continued.

Magnitude	Relational function	Partial expressions	Relative contributions (%)	Overall δ expression	Average δ value
C_L^{corr} $(-)$	$f\left(C_L, \sigma, \epsilon_s\right)$	$\frac{\partial C_L^{corr}}{\partial C_L}\delta C_L$	100	$\left[\left(\frac{\partial C_L^{corr}}{\partial C_L}\delta C_L\right)^2 + \right.$	$4.49{\cdot}10^{-2}$
		$\frac{\partial C_L^{corr}}{\partial \sigma}\delta\sigma$	negligible	$+\left(\frac{\partial C_L^{corr}}{\partial \sigma}\delta\sigma\right)^2 +$	
		$\frac{\partial C_L^{corr}}{\partial \epsilon_b}\delta\epsilon_b$	negligible	$\left. +\left(\frac{\partial C_L^{corr}}{\partial \epsilon_b}\delta\epsilon_b\right)^2\right]^{1/2}$	
C_D $(-)$	$f\left(p, q_\infty, filt\right)$	$\int_{wake}\left(\frac{\partial def}{\partial p}\delta p\right)\mathrm{d}(y')$	negligible	$\int_{wake}\left(\frac{\partial def}{\partial p}\delta p\right)\mathrm{d}(y')+$	$5.17{\cdot}10^{-3}$
		$\int_{wake}\left(\frac{\partial def}{q_\infty}\delta q_\infty\right)\mathrm{d}(y')$	10	$+\int_{wake}\left(\frac{\partial def}{q_\infty}\delta q_\infty\right)\mathrm{d}(y')+$	
		$\int_{wake}(\delta filt)\,\mathrm{d}(y')$	90	$+\int_{wake}(\delta filt)\,\mathrm{d}(y')$	
C_D^{corr} $(-)$	$f\left(C_D, \epsilon_{sb}, \epsilon_s\right)$	$\frac{\partial C_D^{corr}}{\partial C_D}\delta C_D$	100	$\left[\left(\frac{\partial C_D^{corr}}{\partial C_D}\delta C_D\right)^2 + \right.$	$4.97{\cdot}10^{-3}$
		$\frac{\partial C_D^{corr}}{\partial \epsilon_{sb}}\delta\epsilon_{sb}$	negligible	$+\left(\frac{\partial C_D^{corr}}{\partial \epsilon_{sb}}\delta\epsilon_{sb}\right)^2 +$	
		$\frac{\partial C_D^{corr}}{\partial \epsilon_b}\delta\epsilon_b$	negligible	$\left. +\left(\frac{\partial C_D^{corr}}{\partial \epsilon_b}\delta\epsilon_b\right)^2\right]^{1/2}$	

5. Conclusions

The analysis performed herein may be summarized as consisting of two main parts. The former represents an uncertainty analysis following the philosophy of replication levels and performed on a set of basic measurands, i.e. magnitudes that are the direct outputs of an experimental test. In spite of having applied such an analysis to a particular wind tunnel case study, the methodology is meant to be application-agnostic, in the sense that any physical scenario comprising a set of measurement devices should undertake such a task prior to entering a data-production stage. The second part is not as general as the first, and considers the effects that variations in operative conditions may cause on the overall set of magnitudes constituting an experimental test, as well as the propagation of the uncertainty intervals of basic measurands to those of derived magnitudes. This part has two main purposes: firstly, it provides a methodology for quantifying the uncertainties of typical magnitudes related to aerodynamic studies. On this respect, the magnitudes discussed herein are not meant to represent neither an exclusive nor an exhaustive list of parameters, but mainly the ones that the author consider the most relevant. Secondly, it shows how a wrongly controlled experimental procedure leads to values that lie outside the estimated experimental uncertainties.
Regarding the first part, the conclusions to be drawn are:

- 0^{th} order contributions, and system/sensor interactions pertaining the 1^{st} order replication level, may be considered negligible when compared to timewise jitters and calibration errors. The latter, in fact, are shown to be the governing factors of most basic measurand uncertainties.

- Certain measurands, as loads or pressures, require specific testing protocols for assessing purely configuration-dependent perturbations. For which in the case presented herein have been found to be negligible.

As for the second part:

- Sustained tunnel operation causes a progressive variation in the ambient conditions, mainly in T_{amb} and RH, due to the convection of heat losses introduced by the power source of the tunnel. These variations entail a number of consequences: first of all, it remarks the need for monitoring both temperature and relative humidity during tests. Although registering the thermal evolution may be a common practice, hygrometers are not, as far as the authors' knowledge is concerned, as typical in wind tunnel set-ups as temperature transmitters. Modelling the fluid as moist air, with the state equations for density and viscosity found in [10, 11], turns necessary in the light of the severe variations that the RH variable undergoes. Additionally, those variations get propagated to the overall set of derived magnitudes, with the temporal evolutions of the variables directly dependent on T_{amb} and RH being modulated by those signals. The corollary of such influences is that achieving Reynolds constancy during tests becomes a harder task than simply keeeping a predetermined testing velocity.

- The propagation of basic uncertainty intervals to derived magnitudes is shown to have a number of main contributors for each of the magnitudes, as observed in Table 3. However, the factor that determines the uncertainty interval may not be the one governing the evolution of the average values. Thus, in case of the corrected velocity, the interval is wholly dependent on the measured velocity's uncertainty, but T_{amb} and p_{amb} are responsible of introducing a bias-like shift on the data and shaping the curve's temporal evolution. In cases such as the Reynolds number, the interval grows as wide as for being able to subsume the temporal variations of the average values. However, the analysis is performed on the basis of a constant testing velocity. Higher inflow speeds, which are plausible, require increasing the fan's power, with the resultant heat losses and enhanced convection. This, in turn, may cause steeper variations in the average values, and the temporal evolution may become the predominant factor.

- Characteristic lift and drag curves, when obtained under conditions of constant or changing Reynolds numbers, show divergencies that stem from the varying q_∞ values in case operative conditions are not controlled. These deviations may not pose a problem insofar they do not fall outside the estimated

experimental uncertainties of the coefficients. It is to bare in mind, however, that requiring higher inflow velocities (i.e. steeper variations introduced by the operative conditions) or sustaining larger environmental variations may turn the situation critical. In fact, when considering the highly plausible hypothesis that the environmental variations are twice as large as the ones presented in Figure 4, it is shown that the resultant deviations turn the average values unacceptable, mainly for large operative time-lapses. Additionally, those deviations are shown to change non-linearly with the variations in environmental conditions that, ultimately, produce them. Anyhow, the need for monitoring the mentioned variations becomes mandatory for achieving controlled testing conditions.

6. Acknowledgements

The authors gratefully acknowledge the financial support from the Department of Education of the Basque Government for the Research Grant [PRE_2017_1_0178], the Research Group [No. IT009-16] and the Research Project FLUXGARBI [PUE2019-12]. Similarly, they acknowledge the financial support from the Council of Gipuzkoa for the Research Project FETRAFLU [2018-CIEN-000101-01].

References

[1] J. S. Kline and F. A. McClintock. Uncertainties in single-sample expreiments. *Mech. Eng.*, pages 3–8, 1953. ISSN 15821838.

[2] R. J. Moffat. The measurement chain and validation of experimental measurements. In *Acta Imeko, Proc. 6th Congr. Int. Meas. Confed.*, volume 1, pages 45–53, Dresden, Germany, 1973.

[3] R. J. Moffat. Contributions to the Theory of Single-Sample Uncertainty Analysis. *J. Fluids Eng.*, 104:250–258, 1982. ISSN 00332720.

[4] R. J. Moffat. Using Uncertainty Analysis in the Planning of an Experiment. *J. Fluids Eng.*, 107:173–178, 1985. ISSN 00982202.

[5] R. J. Moffat. Describing the Uncertainties in Experimental Results. *Exp. Therm. Fluid Sci.*, 1:3–17, 1988. ISSN 08941777.

[6] Hugh W. Coleman and Glenn Jr. Steele. *Experimentation, Validation, and Uncertainty Analysis for Engineers*. John Wiley & Sons, Ltd, 2009. ISBN 9780470485682.

[7] Jewel B. Barlow, William H Rae, and Alan Pope. *Low-speed wind tunnel testing*. John Wiley & Sons, Inc., 3 edition, 1999. ISBN 0471557749.

[8] José Meseguer-Ruiz and Ángel Sanz-Andrés. *Aerodinámica básica*. Garceta grupo editorial, 2 edition, 2012.

[9] G. Ananda. *Aerodynamic performance of low-to-moderate aspect ratio wings a low Reynolds numbers*. PhD thesis, University of Illinois at Urbana-Champaign, 2012.

[10] A. Picard, R. S. Davis, M. Gläser, and K. Fujii. Revised formula for the density of moist air (CIPM-2007). *Metrologia*, 45(2):149–155, 2008. ISSN 00261394.

[11] Allan J Zuckerwar and Roger W Meredith. Low-frequency absorption of sound in air. *Journal of Acoustical Society of America*, 78(September):946–955, 1985.

[12] Michael Selig, Robert Deters, and Gregory Wiliamson. Wind Tunnel Testing Airfoils at Low Reynolds Numbers. (January), 2014.

[13] Large spanwise variations in profile drag for airfoils at low Reynolds numbers. In *13th Applied Aerodynamics Conference*, volume 33, pages 174–184, 1995. ISBN 9781563471230.

[14] Timothy T. Takahashi. On the decomposition of drag components from wake flow measurements. In *35th Aerospace Sciences Meeting and Exhibit*, number January, Reno, NV, U.S.A, 1997. American Institute for Aeronautics and Astronautics (AIAA).

[15] Ivan Torrano. *Low speed wind tunnel design, setup, validation and testing of airfoils in turbulent in ow conditions*. PhD thesis, Mondragon Goi Eskola Politeknikoa, 2016.

[16] M. A. González, J. M. Ezquerro, V. Lapuerta, A. Laverón, and J. Rodríguez. Components of a Wind Tunnel Balance: Design and Calibration. *Wind Tunnels Exp. Fluid Dyn. Res.*, pages 1–20, 2011. ISSN 9789533070865.

[17] Eckert. D. Correction of support influences on measurements with sting mounted wind tunnel models. Technical report, AGARD, Brussels, Belgium, 1993.

[18] M. Mokry. Evaluation of combined wall- and support-interference on wind tunnel models. Technical report, AGARD, Brussels, Belgium, 1993.

[19] Cameron Tropea, Alexander L. Yarin, and John F. Foss. Pressure Measurement Systems. In *Springer Handb. Exp. Fluid Mech.*, chapter 4, pages 179–214. Springer, Berlin, 1 edition, 2007. ISBN 978-3-540-25141-5.

[20] Chun Fui Liew, Danielle DeLatte, Naoya Takeishi, and Takehisa Yairi. Recent Developments in Aerial Robotics: A Survey and Prototypes Overview. 2017.

- A breakdown of the uncertainty analysis of measurands providing individual contributions.
- Operative condition variations take aerodynamic coefficients outside uncertainty intervals.
- Temperature variations due to wind tunnel operation constitute the critical factor.
- The effect of operative condition variations on aerodynamic coefficients is non-linear.
- An analysis of the operative conditions is to be performed regardless of the experimental set-up.

Graphical Abstract (for review)

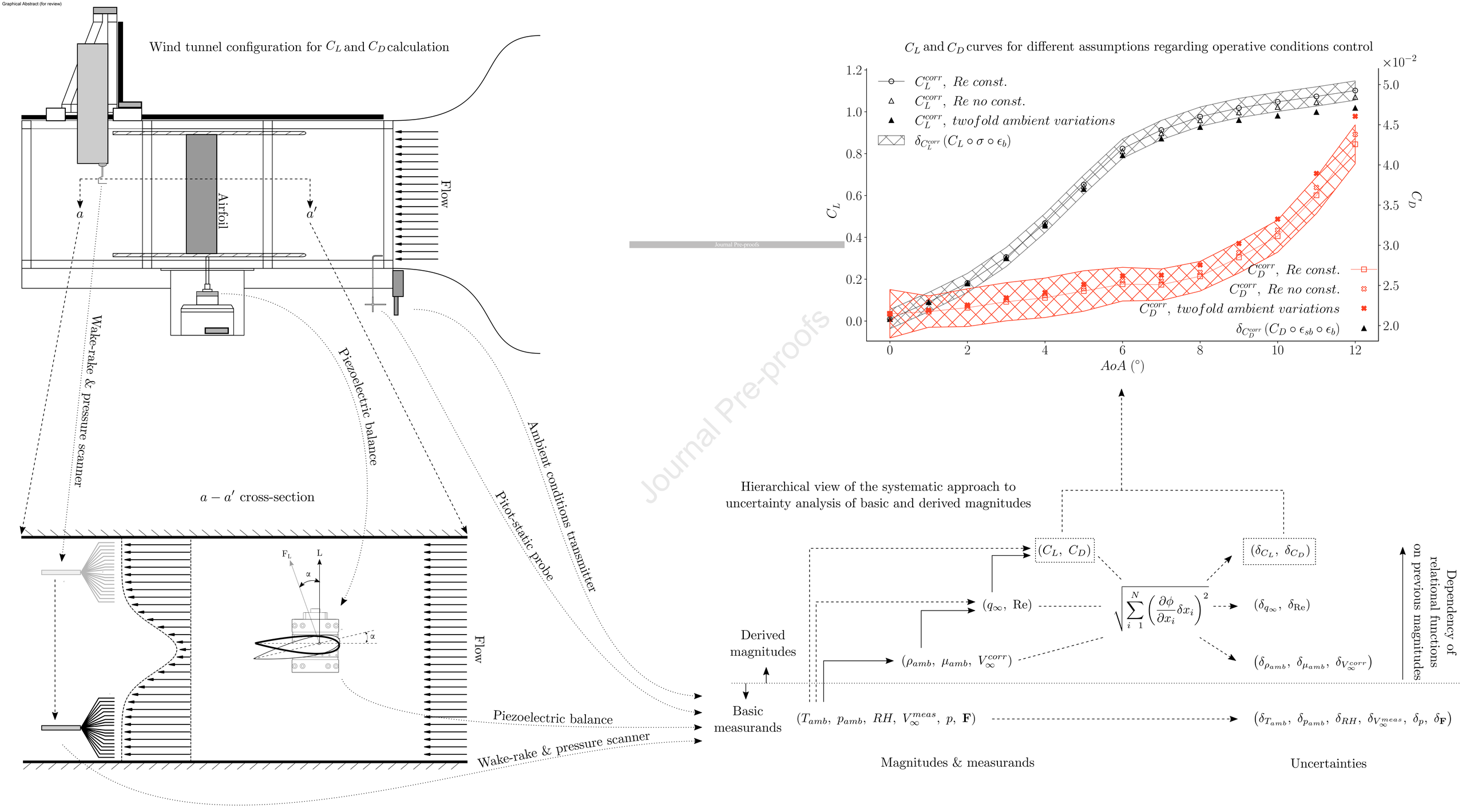

Ander Zarketa-Astigarraga: Conceptualization, Methodology, Software, Validation, Formal Analysis, Investigation, Data Curation, Writing – Original draft, Writing – Review & Editing, Visualization

Alain Martin-Mayor: Conceptualization, Methodology, Resources, Writing – Review & Editing, Supervision, Project Administration, Funding Acquisition

Manex Martinez-Agirre: Conceptualization, Methodology, Resources, Writing – Review & Editing, Supervision, Project Administration, Funding Acquisition

Declaration of interests

☒ The authors declare that they have no known competing financial interests or personal relationships that could have appeared to influence the work reported in this paper.

☐The authors declare the following financial interests/personal relationships which may be considered as potential competing interests: